Incoherent Feedforward Control Governs Adaptation of Activated Ras in a Eukaryotic Chemotaxis Pathway

Kosuke Takeda[1], Danying Shao[2], Micha Adler[3], Pascale G. Charest[1], William F. Loomis[1], Herbert Levine[2], Alex Groisman[3], Wouter-Jan Rappel[2] and Richard A. Firtel[1].

[1] Section of Cell and Developmental Biology, Division of Biological Sciences,

[2] Department of Physics and

[3] Center for Theoretical Biological Physics

University of California, San Diego

La Jolla, CA 92093

Abstract

Adaptation in signaling systems, during which the output returns to a fixed base-amount following a change in the input, often involves negative feedback loops and plays a crucial role in eukaryotic chemotaxis. We determined the dynamical response of a eukaryotic chemotaxis pathway immediately downstream from G protein-coupled receptors following a uniform change in chemoattractant concentration. We found that the response of an activated Ras shows near perfect adaptation. We attempted to fit the results using mathematical models for the two possible simple network topologies that can provide perfect adaptation. Only the incoherent feedforward network was able to accurately describe the experimental results. This analysis revealed that adaptation in this Ras pathway is achieved through the proportional activation of upstream components and not through negative feedback loops. Furthermore, these results are consistent with a local excitation, global inhibition mechanism for gradient sensing, possibly with a RasGAP as a global inhibitor.

Introduction

Many biological systems that exhibit perfect adaptation employ an integral control strategy in which a buffering component of the signaling network integrates the difference between the response and desired basal amount. This difference is then fed back to achieve perfect adaptation through negative regulation. Examples include bacterial chemotaxis (*1-4*), yeast osmoregulation (*5*), and calcium homeostasis in mammals (*6*). Integral control, however, is not the only way to accomplish perfect adaptation. A systematic computational analysis of a three-node network revealed that a second network topology can achieve robust perfect adaptation (*7, 8*). This topology employs an incoherent feedforward mechanism (*9*) in which two nodes of the network are activated proportionally by the input stimulus. These two nodes then act on the third node with opposite effects (such that one activates and one inhibits), leading to a transient response that adapts perfectly. To date, no clear examples of biological networks that use the incoherent feedforward strategy have been identified, which is perhaps surprising because networks that contain incoherent feedforward loops perform better than those that employ integral control (*8*).

Many eukaryotic cells can respond to steep or shallow chemoattractant gradients over a wide range of chemoattractant concentrations (*10, 11*). Not surprisingly, adaptation has been suggested to be a key component of eukaryotic chemotaxis and to be essential for gradient sensing (*12-15*). Indeed, many downstream biochemical components involved in the chemotaxis pathways display adaptive behavior (*16-18*). The precise mechanism of this adaptation, however, is not clear although it occurs downstream from the chemoattractant receptors and coupled heterotrimeric G proteins (*19*). Furthermore, even though many components of the chemotactic pathways have been described, the precise mechanisms of gradient sensing are not fully understood. A number of models for the initial response to gradients have been proposed, most

of which contain a global inhibitor that provides communication between the different parts of the cell (*12, 13, 20-23*). It remains a challenge to distinguish between the different proposed mechanisms in the absence of quantitative data for the kinetics of the underlying pathways.

Results

To measure the adaptation kinetics of a eukaryotic chemotaxis signaling pathway, we exposed cells of the social amoeba *Dictyostelium discoideum* to sudden uniform (global) increases and decreases in the concentration of the chemoattractant cAMP using a microfluidic device (Fig. 1A and fig. S1). We examined the dynamics of activated Ras, Ras-GTP, with the Ras binding domain of human Raf1 (RBD-GFP) as a reporter, which preferentially measures activated RasG, the upstream activator of PI3K (*15, 24, 25*). Ras proteins are molecular switches that bind to and activate downstream effectors in their activated GTP- but not GDP-bound state, with different Ras proteins activating a range of effectors. Ras proteins are activated by RasGEFs (guanine nucleotide exchange factors), which exchange Ras-bound GDP for GTP, and are inactivated by a slow, intrinsic GTPase activity which can be stimulated $>10^3$ fold by RasGAPs (GTPase activating proteins). In unstimulated cells, RasG-GDP is distributed uniformly along the plasma membrane. Following the sudden exposure to a chemotactic gradient, RasG is rapidly and locally activated within seconds at the front of the cell (*24*). This is followed by the Ras-GTP-dependent activation of phosphoinositide 3-kinase (PI3K) and the translocation of PI(3,4,5)P_3 (PIP_3)-binding PH domains to the sites of RasG activation (*24, 26-28*). Activation of RasG, and a second Ras, RasC, at the leading edge of chemotaxing cells is the earliest measurable signaling event downstream of heterotrimeric G protein activation in a sequence of

spatially-localized cellular redistributions of signaling molecules that eventually lead to chemotactic motility (*24, 29-31*).

Using a microfluidic device (fig. S1), we switched the chemoattractant concentration in the medium surrounding the cells within <1 second (Fig. 1B). Multiple cells were imaged every 0.63 s using spinning disk confocal microscopy and the dynamics of activated Ras was followed by the translocation of RBD-GFP to the cell cortex (Fig. 1C). We quantified the dynamics of Ras-GTP by selecting a cytosolic region of interest and measured the RBD-GFP intensity normalized by the average cytosolic intensity before cAMP stimulation and corrected for bleaching as a function of time (Fig. 1D). Prior to changes in chemoattractant concentration, RBD-GFP was uniformly distributed in the cytosol, with a low, basal amount at the plasma membrane. Following an increase in chemoattractant concentration, RBD-GFP translocated rapidly to the cell membrane by binding to Ras-GTP, reaching a maximum at ~3 s. This was followed by a more gradual return to the cytosol where the RBD-GFP intensity returned to its basal amount in <35 s. We verified that the intensity of membrane-associated RBD-GFP was inversely related to cytosolic RBD-GFP fluorescence, further illustrating the translocation of RBD-GFP from cytosol to the membrane and back (fig. S2).

We quantified the degree of adaptation of Ras-GTP by exposing previously unstimulated cells to different chemoattractant concentrations, ranging from 1.0×10^{-2} to 1.0×10^{3} nM (Fig. 2A). The response increased for increasing concentrations and saturated by 1 μM of chemoattractant. Furthermore, the peak time, T_{peak}, defined as the time from the addition of the stimulus to the peak of the response, decreased with increasing concentration of chemoattractant, consistent with previous experiments on the kinetics of PIP_3, a signaling component downstream from activated Ras (*32*). By 35 s, the normalized RBD-GFP amount returned to the pre-stimulus

amount for all chemoattractant concentrations (Fig. 2B), indicating that Ras-GTP adaptation was near perfect over a wide range of stimuli.

To futher quantify the adaptation kinetics of Ras-GTP, we exposed cells to a constant chemoattractant concentration for 10 min, followed by a sudden increase in chemoattractant concentration. We computed the response (maximum decrease in cytosolic RBD-GFP fluoresence), I_{peak}, which reflects the translocation of the reporter to the membrane. These values were normalized by the maximum response in naïve (not pre-treated) cells following a 1 μM stimulus (Fig. 2C). Cells that were not pre-treated with cAMP responded to a chemoattractant increase that spanned 3-4 orders of magnitude with an EC_{50} of approximately 0.25 nM. Furthermore, cells that were pre-treated with 100 nM showed a considerable response to a sudden increase in stimulus. T_{peak}, which, for the four different pre-stimulus amounts, decreased with increasing chemoattractant (Fig. 2D).

Finally, we examined the Ras-GTP kinetics in cells that were exposed to a sudden increase and a subsequent sudden decrease in cAMP. In the first experiment, the concentration went from 0 nM to 0.2 nM and back to 0 nM (Fig. 2E). As before, the cytosolic RBD-GFP fluorescence decreased (due to translocation of the reporter to the cortex) following the increase in chemoattractant, whereas the decrease in cAMP concentration led to a rapid increase in the cytosolic RBD-GFP fluorescence and a subsequent slow return to the basal amount. In the second experiment, the concentrations changed from 100 nM to 1000 nM and back to 100 nM (Fig. 2F) and compared to the first experiment (Fig. 2E), the return to basal amount after the decrease in cAMP concentration was markedly faster.

Previous studies identified a number of feedback loops that involve activated RasG, PI3K, and F-actin polymerization (*24, 33-36*). To determine the role of the F-actin feedback loop in the

observed adaptation, we treated cells with latrunculin B to block F-actin polymerization. Again, we found that the cytosolic RBD-GFP amounts returned to basal amounts following a sudden change in chemoattractant concentration, indicating adaptation was not affected (fig. S3). Furthermore, latrunculin B treatment did not have a major effect upon either the dose reponse curve (Fig. 2G) or the characteristic response time (Fig. 2H). These results show that RasG adaptation does not involve feedback loops containing actin and that the signaling network resposible for the observed perfect adaptation is upstream from F-actin polymerization.

This finding, combined with previous experimental results that demonstrate that adaptation occurs downstream from the receptors (*19*), motivated us to construct a mathematical model for adaptation that contained only Ras-GTP, RasGEF, and RasGAP. To determine which network topology is consistent with our experimental data, we constructed models that incorporate the two known three-node network topologies that can produce perfect adaptation (Fig. 3, A and B) (*7, 8*). In the incoherent feedforward topology, both the RasGEF and the RasGAP are activated by the chemoattractant signal acting through the receptors R (Fig. 3A). Because RasGEF and RasGAP activate and inhibit Ras respectively, this network can have the properties of ultrasensitivity described by Goldbeter and Koshland (*37*). In the integral control topology, the output of the model, Ras-GTP, is fed back using the RasGAP as a buffering node (Fig. 3B). In both models, the external stimulus is translated into an internal response through the binding of the chemoattractant cAMP to the receptors.

Previous studies have identified several species of receptors with different binding affinities for cAMP (*38*). Thus, we included two types of receptors in our models, one with a high affinity (R_1, with a dissociation constant of K_d^1=60nM) and one with a low affinity (R_2, with a

dissociation constant of K_d^2=450nM). We assumed that the two types of receptors activate downstream components in an identical fashion. Numerical fits with only one receptor population resulted in dose-response curves that were less accurate (text S1 and fig. S4).

These models can be cast in terms of ordinary differential equations (text S2) that can be integrated in time to determine the dynamical response for various temporal patterns of the stimulus as a function of changes in the amount of stimulus. To compare the dynamic response of the two topologies to the experimental results, we performed mathematical fits using a subset of the experimental data. Specifically, we used the dose response curves (Fig. 2C), the response time curves (Fig. 2D), and the peak times and amplitudes following the decrease in cAMP concentration and the response amplitude 60 s after the decrease (Fig 2, E and F). We employed a simulated annealing fitting procedure (text S3) and, to avoid overfitting the data, used only two data sets, non-pretreated cells and cells pretreated with 100 nM chemoattractant (Fig. 2, C and D). The resulting numerical fit using 21 data points constrained the 9 free model parameters in both topologies. Our simulation results indicated that the integral control mechanism was incompatible with our experimental results. In particular, this mechanism displayed considerable dependence of the adaptation kinetics on the size of the stimulus step (Fig. 3C). Contrary to our experimental results, for small concentration increases this network led to oscillations and time to reach the basal amount increased markedly as the step size increased (fig. S5). This dependence could be analyzed analytically (fig. S5). Additionally, other ways to implement integral control are also incompatible with the experimental data (fig. S6).

The results of the best fit using the incoherent feedforward network are shown as solid lines in Fig. 2, C and D. In contrast to the integral control topology, the RBD-GFP amount in the incoherent feedforward model could respond to a wide range of concentrations of

chemoattractant stimuli and adapted quickly. Specifically, this network topology could respond quickly even when the stimulus was large. Furthermore, the numerical results track the experimental data well for all stimulus strengths, including the data sets that were not explicitly fitted. The model parameters obtained by our fitting procedure are listed in Table S1.

A closer inspection of the results of our fitting procedure revealed that the activation kinetics of RasGEF were faster than that of the RasGAP. This is to be expected since a positive Ras-GTP response following an increase in cAMP requires that the activation step initially is larger than the de-activation step. Eventually, the RasGAP kinetics catches up, resulting in a steady-state Ras-GTP amount that is independent of the stimulus strength. The kinetics of our model components is shown in Fig. 3D where we plot RasGAP, RasGEF, and Ras-GTP as a function of time, following a sudden increase in chemoattractant concentration. In Fig. 3E, we plot the full dynamical response in our simulations together with experimental results for two jumps in the chemoattractant concentration. Finally, our simulation results for the two experiments in which the concentration is increased and then subsequently decreased are shown as solid lines in Fig. 2, E and F. The agreement between the experiments and the simulations is excellent for the entire time course of the experiments.

Discussion

Our study examined the initial response to changes in uniform chemoattractant stimuli using a combined experimental and theoretical approach. We did not consider possible responses with longer time scales, including the formation of Ras patches (localized areas of increased concentration of membrane bound Ras-GTP) and cell polarization. We find that the response of activated RasG adapted perfectly for a large range of cAMP stimuli, in particular for stimuli less

than 1 μM. The inclusion of GEF saturation in our model could account for the possibe deviation from perfect adaptation for very large stimuli (text S2). We also found that the peak time of the response of activated RasG decreases with increasing stimulus concentration. This is consistent with previous experiments on the kinetics of membrane-bound PIP_3, a signaling component downstream from activated Ras, which showed that the peak value for PIP_3 is reached faster for a high value of cAMP stimulus (100 nM) that for a low value of cAMP (1 nM) (*32*).

Our combined experimental and theoretical analysis suggests that adaptation in the RasG signaling pathway does not rely on integral control mechanisms that contain negative feedback loops. Instead, and unlike any other biological systems analyzed to date, adaptation is achieved through the simultaneous activation of an activator and inhibitor. In the model we have analyzed here, the signal directly activates RasGEF and RasGAP and variants of the incoherent feedforward topology (fig. S7) will give similar results. Of course, an alternate possibility is that adaptation is achieved downstream from the receptors and upstream from RasGEF. The output of this adaptation module, containing unknown components, would then activate RasGEF while RasGAP is constitutively active. In either case, our network is consistent with the local excitation, global inhibition (LEGI) model (*12*) for gradient sensing that postulates that the response to an external chemoattractant signal is governed by an intracellular membrane-bound activator and a diffuse inhibitor throughout the cell. Such a gradient sensing model can convert the external gradient of bound receptors into an internal gradient, especially if it is coupled to a module that further amplifies the internal asymmetry (*39, 40*). Our model suggests that the activator RasGEF is the local, membrane bound component whereas the inhibitor RasGAP is the diffuse cytosolic component. This is consistent with previous results showing that the RasG-GAP *Dictyostelium* NF1 is an essential and uniformly distributed component of the directional

sensing mechanism and that in the absence of NF1, cells are unable to effectively sense the chemoattractant gradient's direction and exhibit extended RasG activation (*15*). Further, our results argue that the RasG-GAP is not constitutively active but is activated in response to chemoattractant stimulation and that this activation of both the RasGEF and the RasGAP is essential for gradient sensing and adaptation.

Materials and Methods

Growth and development.

Transformed KAx-3 cells carrying an extrachromosomal construct in which the regulatory region of Actin 15 drives a fusion of GFP to the Ras binding domain of Raf were grown in suspension in HL5 medium. When exponentially growing cells reached 1-3 x 10^6 cells/ml, they were harvested by centrifugation, washed in phosphate buffer, and resuspended in phosphate buffer at 5 x 10^6 cells/ml. Shaken cells were starved for 1 hour before addition of pulses of 30 nM cAMP every 6 min for 5 hours.

Temporal stimulation.

Developed cells were harvested, washed twice with phosphate buffer, and loaded into microfluidic test chambers using a syringe and a blunt canula. Cells were allowed to settle and disperse on the coverslip at the bottom of the test chambers for 15-30 min before imaging and stimulation. Before and during the exposure to cAMP, the cells were under the same continuous shear flow of fresh medium, preventing the effect of self-secreted cAMP and of stimulation by shear. Fluorescence images were taken every 0.63 sec using a Leica inverted confocal microscope with a 63X/1.4 objective and a Hamamatsu EM-CCD camera. Alexa594 (Invitrogen) fluorescent dye was added to the cAMP solutions used to monitor cAMP temporal change.

Microfluidic device and setup.

The microfluidic device used in the study consisted of a polydimethylsiloxane (PDMS) chip with microchannels engraved on its surface and a #1.5 microscope cover glass sealing the microchannels (Fig. 1A and fig. S1). Its major elements were 5 observation chambers, each situated upstream of a dedicated outlet, a mixing channel, and resistance channels. The mixing channel served the purpose of mixing the buffer flowing from the buffer inlet with a concentrated cAMP solution flowing from the cAMP inlet to deliver to the observation chambers a well-mixed solution with a reduced concentration of cAMP. Steps of cAMP concentration with a transition time of ~0.25 sec were generated by switching the pressure at the cAMP inlet with a solenoid valve.

Fluorescence Microscopy Methods.

A series of confocal images of a 115 μm x 115 μm (512 x 512 pixels) region were recorded (SimplePCI) and saved as 16-bit grayscale bitmaps. The images were processed in ImageJ by selecting, for each cell, a cytosolic region of interest with the aid of a computer. To determine the cytosolic region, we used a customized plug-in for ImageJ, which automatically outlined the cell perimeter. This perimeter was shrunk by 2 pixels, resulting in the cell interior. Visible cytosolic organelles, defined as areas of very low or very high fluorescence intensity, were omitted. The fluorescence signal for the image at time t, $I_c(t)$, was determined by taking the average value of all pixels within the cell interior. We also determined the average cytosolic fluorescence intensity, I_{c0}, during the 18 frames immediately preceding cAMP stimulation. The fluorescence signal was then normalized by computing the following value: $I_{c,nor}(t)=(I_c(t)-I_b)/(I_{c0}-I_b)$, where I_b is the background fluorescence intensity. For each experiment, the fluorescent signal was also

corrected for bleaching effects. These bleaching effects typically account for ~10% intensity loss during a 1 min recording. For the correction, we determined the cytosolic fluorescence signal I_a for each cell in the absence of any stimulation during a time interval that was identical to the one corresponding to the duration of the experiment. This signal was processed as the signal in the actual experiment, resulting in a normalized time-series $I_{a,nor}(t)=(I_a(t)-I_b)/(I_{a0}-I_b)$. The final cytosolic signal, as reported in this study, was then computed as $I(t)=I_{c,nor}(t)/I_{a,nor}(t)$.

Supplementary Materials:

Text S1: Effects of two species of receptors

Text S2: Model equations.

Text S3: Data fitting.

Text S4. Analytical analysis of the incoherent feedforward and the integral control topologies.

Text S5. Spatially extended models.

Fig. S1. Detailed drawing of the microfluidic device

Fig S2. Membrane-associated RBD-GFP is inversely related to cytosolic RBD-GFP fluorescence.

Fig. S3. Responses in latrunculin-treated cells.

Fig. S4 Effects of different receptor populations.

Fig. S5. Response time for the different models.

Fig. S6. Possible integral control topologies.

Fig. S7. Possible incoherent feedforward topologies.

Fig. S8. Core model topologies.

Fig. S9. Comparison of the response in a spatially uniform and spatially extended model.

Table S1. Model parameters used in this study.

Fig. 1. A sudden change in uniform chemoattractant results in a transient reponse of RBD-GFP to the membrane. **(A)** Drawing of channels of the microfluidic device employed in our experiments. **(B)** The concentration in a test chamber of the device is switched within 1 s, as demonstrated by recording the fluorescence intensity of a dye. **(C)** Images of a *Dictyostelium* cell undergoing a sudden increase in cAMP concentration at t=0 s. **(D)** The cytosolic

fluorescence intensity of RBD-GFP, normalized by the fluorescent intensity before stimulation and corrected for bleaching, as a function of time following a sudden 1 μM cAMP increase at t=0 s. The amplitude of the maximum response, I_{peak}, and its time point, T_{peak}, were recorded for each experiment.

Fig. 2. Ras response adapts over a large range of concentrations. **(A)** The RBD-GFP cytosolic fluorescence intensity I(t) as a function of time for different amounts of stimulation. **(B)** The cytosolic fluorescence intensity of RBD-GFP after 35 s as a function of the cAMP concentration. **(C)** The RBD-GFP dose-response curves for different pre-treatment concentrations. The x-axis represents the post-stimulation concentration of the chemoattractant. The symbols are the experimental results. The solid lines are the results of our numerical simulations using the incoherent feedforward network. The error bars here, and elsewhere in this paper, represent the standard deviation. **(D)** The time of the maximum RBD-GFP response for different pre-stimulation and stimulation amounts of cAMP (experiments: symbols, simulations: solid lines). **(E)** and **(F)** I(t) as a function of time following a sudden increase (at 15 s) and a sudden decrease (at 75 s) of cAMP concentration. The symbols correspond to the experimental results while the solid lines represent our numerical results. In (E), the concentration increased from 0 to 0.2 nM, then decreased back to 0 nM. In (F), cells were exposed to 100 nM, followed by a sudden increase to 1 μM and a subsequent drop back to 100 nM. **(G)** The dose response curve for untreated cells following a sudden increase of cAMP with (red) and without latrunculin B (black). **(H)** The peak time of the response as a function of cAMP concentration with (red line) and without latrunculin B (black line). (B), (C), (D), (G), and (H) represent the average response of N=60 cells from three independent experiments.

Fig. 3. One network topology is consistent with the experimental data. **(A)** The incoherent feedforward model of Ras adaptation considered in this study. The chemoattractant binds to G-

protein coupled receptors, leading to the activation of both RasGEF and RasGAP which activates and inactivates Ras, respectively. **(B)** An implementation of the integral control topology. The receptor activates a RasGEF which, in turn, activates Ras. The RasGAP is activated by Ras-GTP and, through negative feedback, inactivates Ras, thus functioning as a buffering node. **(C)** The response of the integral control network, normalized to the pre-stimulus RBD-GFP concentration, for different amounts of chemoattractant stimulation. **(D)** A typical time course of the RasGAP, RasGEF, and Ras-GTP for the incoherent feedforward model following a sudden increase in chemoattractant at 0 s. **(E)** The full dynamical response of RBD-GFP in the experiments (symbols) and in the fitted model (solid lines) for two different concentration increases.

References and Notes

1. H. C. Berg, D. A. Brown, Chemotaxis in Escherichia coli analysed by three-dimensional tracking. *Nature* **239**, 500 (Oct 27, 1972).
2. N. Barkai, S. Leibler, Robustness in simple biochemical networks. *Nature* **387**, 913 (Jun 26, 1997).
3. T. M. Yi, Y. Huang, M. I. Simon, J. Doyle, Robust perfect adaptation in bacterial chemotaxis through integral feedback control. *Proc Natl Acad Sci U S A* **97**, 4649 (Apr 25, 2000).
4. R. G. Endres, N. S. Wingreen, Precise adaptation in bacterial chemotaxis through "assistance neighborhoods". *Proc Natl Acad Sci U S A* **103**, 13040 (Aug 29, 2006).
5. D. Muzzey, C. A. Gomez-Uribe, J. T. Mettetal, A. van Oudenaarden, A systems-level analysis of perfect adaptation in yeast osmoregulation. *Cell* **138**, 160 (Jul 10, 2009).
6. H. El-Samad, J. P. Goff, M. Khammash, Calcium homeostasis and parturient hypocalcemia: an integral feedback perspective. *J Theor Biol* **214**, 17 (Jan 7, 2002).
7. M. Behar, N. Hao, H. G. Dohlman, T. C. Elston, Mathematical and computational analysis of adaptation via feedback inhibition in signal transduction pathways. *Biophys. J.* **93**, 806 (2007).
8. W. Ma, A. Trusina, H. El-Samad, W. A. Lim, C. Tang, Defining network topologies that can achieve biochemical adaptation. *Cell* **138**, 760 (Aug 21, 2009).
9. S. S. Shen-Orr, R. Milo, S. Mangan, U. Alon, Network motifs in the transcriptional regulation

network of Escherichia coli. *Nat Genet* **31**, 64 (May, 2002).
10. D. Fuller *et al*., External and internal constraints on eukaryotic chemotaxis. *Proc Natl Acad Sci U S A* **107**, 9656 (May 25, 2010).
11. L. Song *et al*., Dictyostelium discoideum chemotaxis: threshold for directed motion. *Eur. J. Cell Biol.* **85**, 981 (2006).
12. C. A. Parent, P. N. Devreotes, A cell's sense of direction. *Science* **284**, 765 (1999).
13. A. Levchenko, P. A. Iglesias, Models of eukaryotic gradient sensing: application to chemotaxis of amoebae and neutrophils. *Biophys. J.* **82**, 50 (2002).
14. G. L. Ming *et al*., Adaptation in the chemotactic guidance of nerve growth cones. *Nature* **417**, 411 (May 23, 2002).
15. S. Zhang, P. G. Charest, R. A. Firtel, Spatiotemporal regulation of Ras activity provides directional sensing. *Curr Biol* **18**, 1587 (Oct 28, 2008).
16. P. J. M. van Haastert, P. R. van der Heijden, Excitation adaptation and deadaptation of the cAMP mediated cGMP response in Dictyostelium discoideum. *J. Cell Biol.* **96**, 347 (1983).
17. S. H. Zigmond, S. J. Sullivan, Sensory adaptation of leukocytes to chemotactic peptides. *J Cell Biol* **82**, 517 (Aug, 1979).
18. X. Xu, M. Meier-Schellersheim, J. Yan, T. Jin, Locally controlled inhibitory mechanisms are involved in eukaryotic GPCR-mediated chemosensing. *J. Cell Biol.* **178**, 141 (2007).
19. C. Janetopoulos, T. Jin, P. Devreotes, Receptor-mediated activation of heterotrimeric G-proteins in living cells. *Science* **291**, 2408 (2001).
20. W. J. Rappel, P. J. Thomas, H. Levine, W. F. Loomis, Establishing direction during chemotaxis in eukaryotic cells. *Biophys. J.* **83**, 1361 (2002).
21. H. Levine, D. A. Kessler, W. J. Rappel, Directional sensing in eukaryotic chemotaxis: A balanced inactivation model. *Proc. Natl. Acad. Sci. USA* **103**, 9761 (2006).
22. C. Beta, G. Amselem, E. Bodenschatz, A bistable mechanism for directional sensing. *New Journal of Physics* **10**, 083015 (Aug, 2008).
23. M. Postma, P. J. M. van Haastert, A diffusion-translocation model for gradient sensing by chemotactic cells. *Biophys. J.* **81**, 1314 (2001).
24. A. T. Sasaki, C. Chun, K. Takeda, R. A. Firtel, Localized Ras signaling at the leading edge regulates P13K, cell polarity, and directional cell movement. *J. Cell Biol.* **167**, 505 (2004).
25. H. Kae *et al*., Cyclic AMP signalling in Dictyostelium: G-proteins activate separate ras pathways using specific RasGefs. *EMBO Rep.* **8**, 477 (2007).
26. C. A. Parent, B. J. Blacklock, W. M. Froehlich, D. B. Murphy, P. N. Devreotes, G protein signaling events are activated at the leading edge of chemotactic cells. *Cell* **95**, 81 (1998).
27. R. Meili *et al*., Chemoattractant-mediated transient activation and membrane localization of Akt/PKB is required for efficient chemotaxis to cAMP in Dictyostelium. *EMBO J.* **18**, 2092 (1999).
28. S. Funamoto, R. Meili, S. Lee, L. Parry, R. A. Firtel, Spatial and temporal regulation of 3-phosphoinositides by PI 3-kinase and PTEN mediates chemotaxis. *Cell* **109**, 611 (2002).
29. K. F. Swaney, C. H. Huang, P. N. Devreotes, Eukaryotic chemotaxis: a network of signaling pathways controls motility, directional sensing, and polarity. *Annu Rev Biophys* **39**, 265 (Jun 9, 2010).
30. P. G. Charest, R. A. Firtel, Feedback signaling controls leading-edge formation during chemotaxis. *Curr Opin Genet Dev* **16**, 339 (Aug, 2006).
31. W. J. Rappel, W. F. Loomis, Eukaryotic Chemotaxis. *Wiley Interdiscip Rev Syst Biol Med* **1**, 141 (2009).
32. X. H. Xu, M. Meier-Schellersheim, X. M. Jiao, L. E. Nelson, T. Jin, Quantitative imaging of single live cells reveals spatiotemporal dynamics of multistep signaling events of chemoattractant gradient sensing in Dictyostelium. *Mol. Biol. Cell* **16**, 676 (2005).
33. K. C. Park *et al*., Rac regulation of chemotaxis and morphogenesis in Dictyostelium. *EMBO J.* **23**, 4177 (2004).

34. P. G. Charest *et al*., A Ras signaling complex controls the RasC-TORC2 pathway and directed cell migration. *Dev Cell* **18**, 737 (May 18, 2010).
35. M. Fivaz, S. Bandara, T. Inoue, T. Meyer, Robust neuronal symmetry breaking by Ras-triggered local positive feedback. *Curr Biol* **18**, 44 (Jan 8, 2008).
36. A. T. Sasaki *et al*., G protein-independent Ras/PI3K/F-actin circuit regulates basic cell motility. *J. Cell Biol*. **178**, 185 (2007).
37. A. Goldbeter, D. E. Koshland, Jr., An amplified sensitivity arising from covalent modification in biological systems. *Proc Natl Acad Sci U S A* **78**, 6840 (Nov, 1981).
38. P. J. M. van Haastert, R. J. W. de Wit, Demonstration of receptor heterogeneity and affinity modulation by nonequilibrium binding experiments. The cell surface cAMP receptor of Dictyostelium discoideum. *J. Biol. Chem.* **259**, 13321 (1984).
39. I. Hecht, D. A. Kessler, H. Levine, Transient localized patterns in noise-driven reaction-diffusion systems. *Phys Rev Lett* **104**, 158301 (Apr 16, 2010).
40. Y. Xiong, C. H. Huang, P. A. Iglesias, P. N. Devreotes, Cells navigate with a local-excitation, global-inhibition-biased excitable network. *Proc Natl Acad Sci U S A* **107**, 17079 (Oct 5, 2010).
41. **Acknowledgement:** We thank Peter Van Haastert for providing us with the Raf-GFP cells. **Funding**: This work was supported by the US National Institutes of Health (PO1 GM078586).
Author Contributions: T.K. performed the experiments with assistance from P.G.C. D.S. performed the modeling simulations. M.A. and A.G. designed and fabricated the microfluidic devices. R.A.F. and W.J.R designed the experiments and modeling studies, with contributions from W.F.L. and H.L. The manuscript was written by R.A.F. and W.J.R. with assistance from all other authors.

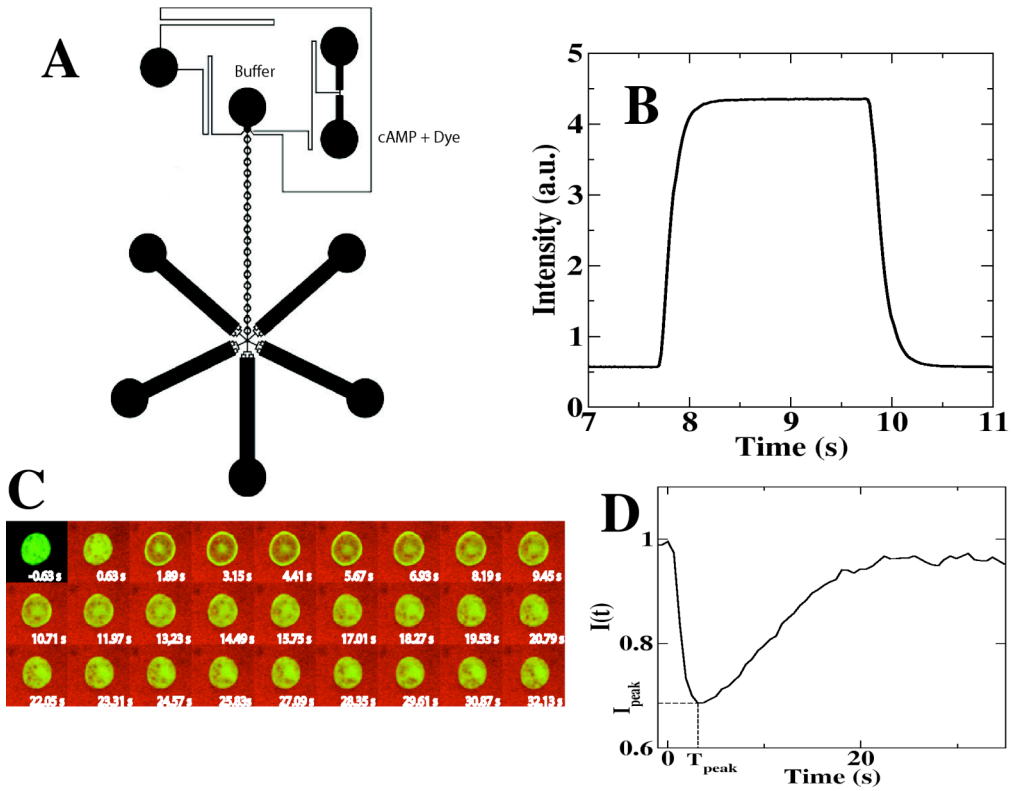

Fig. 1. Sudden change in uniform chemoattractant results in a transient reponse of RBD-GFP to the membrane. **(A)** Drawing of channels of the microfluidic device employed in our experiments. **(B)** The concentration in a test chamber of the device is switched within 1 s, as demonstrated by recording the fluorescence intensity of a dye. **(C)** Images of a Dictyostelium cell undergoing a sudden increase in cAMP concentration at t=0s. **(D)** The cytosolic fluorescence intensity of RBD-GFP, normalized by the fluorescent intensity before stimulation and corrected for bleaching, as a function of time following a sudden 1 μM cAMP increase at t=0s. The amplitude of the maximum response, I_{peak}, and its time point, T_{peak}, are recorded for each experiment.

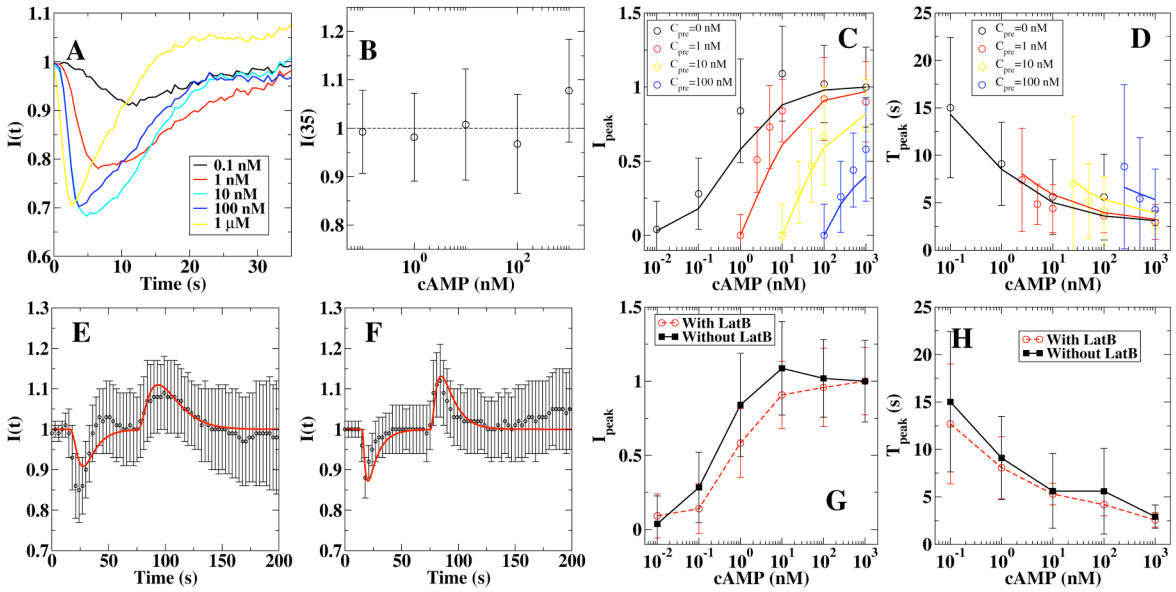

Fig. 2. Ras response adapts over a large range of concentrations. **(A)** The RBD-GFP cytosolic fluorescence intensity I(t) as a function of time for different levels of stimulation. **(B)** The cytosolic fluorescence intensity of RBD-GFP after 35s as a function of the cAMP concentration. Here, and in C, D, G, and H, the results represent the average response of N=60 cells from three independent experiments. **(C)** The RBD-GFP dose-response curves for different pre-treatment concentrations. The x-axis represents the post-stimulation concentration of the chemoattractant. The symbols are the experimental results while the solid lines are the results of our numerical simulations using the incoherent feedforward network. The error bars here, and elsewhere in this paper, represent the standard deviation. **(D)** The time of the maximum RBD-GFP response for different pre-stimulation and stimulation levels of cAMP (experiments: symbols, simulations: solid lines). **(E)** and **(F)**, I(t) as a function of time following a sudden increase (at 15 s) and a sudden decrease (at 75 s) of cAMP concentration. The symbols correspond to the experimental results while the solid lines represent our numerical results. In E, the concentration increased from 0 to 0.2 nM, then decreased back to 0 nM. In F, cells were exposed to 100 nM, followed by a sudden increase to 1 μM and a subsequent drop back to 100 nM. **(G)** The dose response curve for untreated cells following a sudden increase of cAMP with (red) and without latrunculin B (black). **(H)** The peak time of the response as a function of cAMP concentration with (red line) and without latrunculin B (black line).

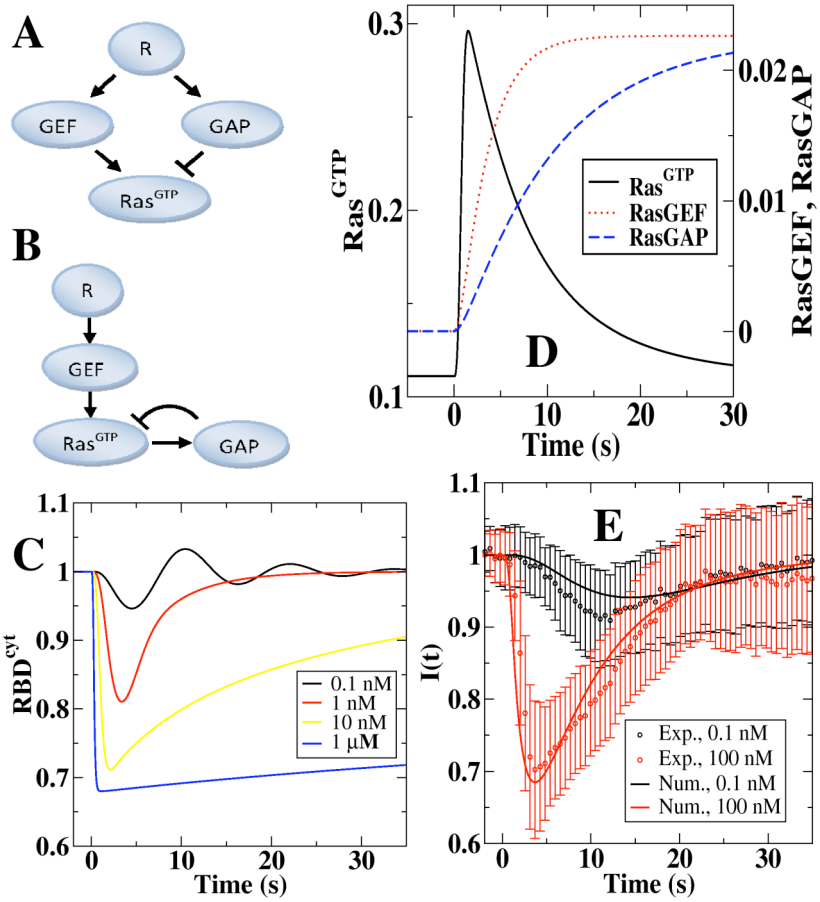

Fig. 3. Only one possible network topology is consistent with the experimental data. **(A)** The incoherent feedforward model of Ras adaptation considered in this study. The chemoattractant binds to G-protein coupled receptors, leading to the activation of both RasGEF and RasGAP which activates and de-activates Ras, respectively. **(B)** An implementation of the integral control topology. The receptor activates a RasGEF which, in turn, activates Ras. The RasGAP is activated by Ras-GTP and, through a negative feedback, inactivates Ras, thus functioning as a buffering node. **(C)** The response of the integral control network, normalized to the pre-stimulus level of RBD-GFP concentration, for different levels of chemoattractant stimulation. **(D)** A typical time course of the RasGAP, RasGEF, and Ras-GTP for the incoherent feedforward model following a sudden increase in chemoattractant at 0 s. **(E)** The full dynamical response of RBD-GFP in the experiments (symbols) and in the fitted model (solid lines) for two different concentration increases.